The 2023 World Congress on
Advances in Structural Engineering and Mechanics (ASEM23)
GECE, Seoul, Korea, August 16-18, 2023

Structural Performance of Column-to-Base Connections of Steel Pole-Mounted Structures

Didar Meiramov[1)], *Hyunjin Ju[2)], Yujae Seo[3)]

[1),3)] *Department of Architecture and Architectural Engineering, Hankyong National University, Anseong 17579, Korea*
[2)] *School of Architectural and Design Convergence, Hankyong National University, Anseong 17579, Korea*

[2)] hju@hknu.ac.kr

ABSTRACT

This study aimed to develop a non-welded plinth for the column-base connection of pole-mounted solar panel structures to have sufficient strength and superior durability. Considering the connection details as a key variable, the load-carrying capacities of 4 welded plinths and 6 non-welded plinths were investigated by experimental and analytical studies. The experimental results indicated that most specimens had sufficient load-carrying capacity to withstand the calculated yielding force. The numerical results demonstrated that the details of the connection, such as the orientation and shape of the side plates, use of rib plates, and bolt layout affected the structural performance. Therefore, the column–base connections should be carefully designed based on proper structural evaluation of the connection details.

1. INTRODUCTION

Large surface areas of solar panels cause the structure to experience a high overturning moment and even collapse under extreme wind loads. Although the average wind speed in South Korea is as low as 4.0 m/s, the maximum wind speed that should be considered in structural design is 54 m/s, which can occur during typhoons (Kim et al., 2019). Meanwhile, the solar panel structure is exposed to harsh environmental conditions, including wind loads, temperature variance, and corrosion. The parts of solar panel structures can be made from high-durability steel (PosMAC; magnesium–aluminum alloy coating product). However, welding connections to PosMAC steel can damage the magnesium–aluminum alloy coating, and the advantage of using PosMAC cannot be obtained in terms of durability (Sohn et al., 2021). Thus, this study investigates

---

[1) & 3)] Graduate Student
[2)] Assistant Professor, *Corresponding author

the structural performance of 4 welded and 6 non-welded column–base connections in a pole-mounted solar panel structure and analyzes the influence of connection details such as the orientation and shape of the side plate, the existence of the base plate, and different bolt layouts on the load-bearing capacity of the structure.

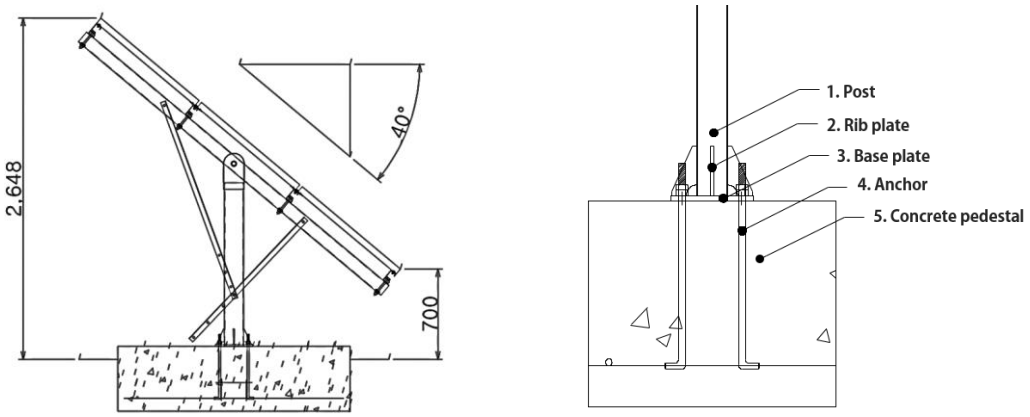

(a) Side view of a solar panel (b) Details of the column-to-base connection

Fig. 1. The representation of the column-base joint of pole-mounted solar structures

2. EXPERIMENTAL SCHEME

The welded plinths are constructed by welding the side plate to the base plate, whereas the non-welded plinths without a separate base plate consist of a supporting plate unit formed by bending the side plate or assembled by welding steel plates to obtain the unified base with side plate, as presented in Table 1. All of the specimens have bolted connections between the post and side plates, except for welded rib plate reinforced (WRR) specimen.

Loading was applied to column–base connections that were symmetrically connected as if two cantilevers were loaded on one hinge and one fixed-end boundary condition, as shown in Fig. 1. The test specimen was supported by hinges located 100 mm from both ends to constrain the posts in the horizontal and vertical directions and allow free rotation at the post ends. The loading was applied upward at the mid-span of the assembly, which is the location of the symmetrically connected column–base connections, as shown in Fig. 1. The displacements and strains at critical regions of the specimens were measured during the tests.

Table 1. Detailed information about the plinths

Name	Connection	Shape	Name	Connection	Shape
WRR	welded	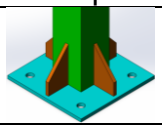	TC	non-welded	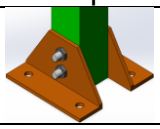

SWP	welded	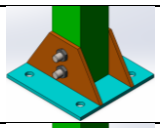	TCR	non-welded	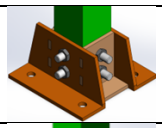
UC	welded	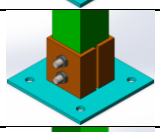	TUC	non-welded	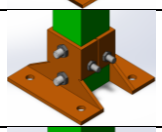
SC	welded	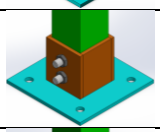	BSP	non-welded	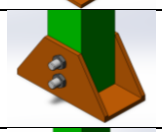
URC	non-welded	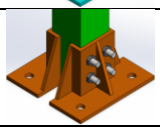	LC	non-welded	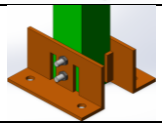

Note: URC – U-shaped rib plate reinforced, TC – trapezoidal plate connection, TCR – trapezoidal plate connection with reinforcement, TUC – trapezoidal U-shaped plate connection, BSP – bent side plate, LC – L-shaped plate connection.

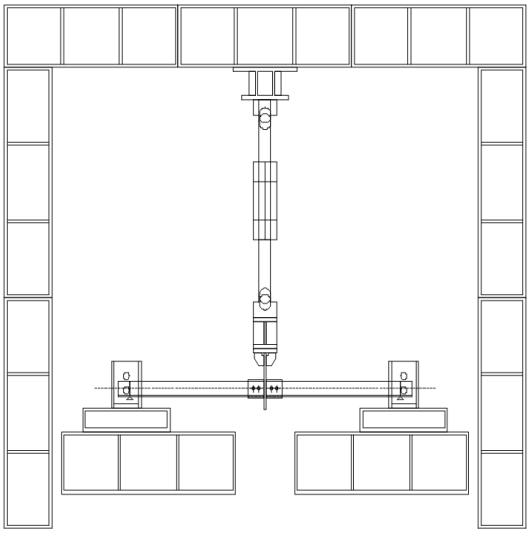

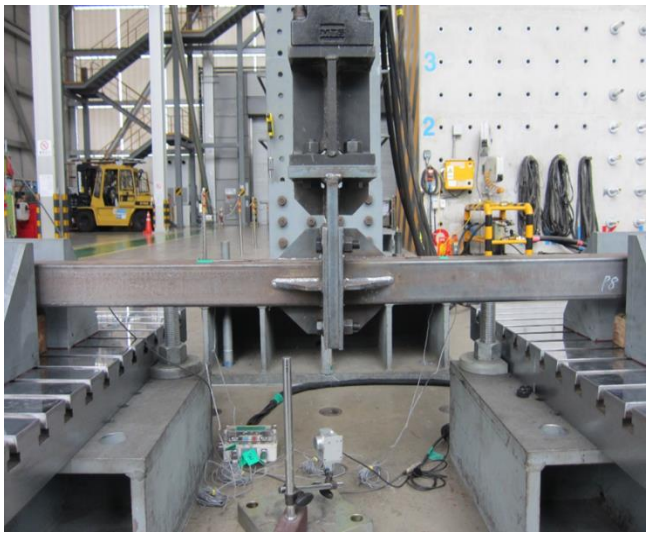

(a) Schematic of experimental apparatus (b) WRR specimen under loading

Fig. 2. Experimental setup

3. NONLINEAR FINITE ELEMENT ANALYSIS

A finite element model was developed considering geometric and material nonlinearities using ANSYS 2022 R2 Static Structural to verify the simulation results by comparing them with the experimental data. Additionally, a parametric study was conducted on the orthogonal axes of plinths to investigate the structural performances of the column–base connections along the strong and weak axes according to the connection details using the verified model. Bonded contact was assigned to the welded regions, while a combination of frictionless and bonded contacts was assigned for bolted connections. As shown in Fig. 3, a fine mesh of solid elements with a size of 11 mm was

employed in the region where failure or buckling could occur. In addition, an even finer mesh of 3 mm was applied to the bolted connections and the surrounding steel plate to obtain accurate results of the bolt behaviors.
Before assigning the material properties of each part of the assembly, the stress-strain relationship from the test results was converted to a true stress-strain curve, as follows:

$$\sigma_{true} = \sigma_{eng} * (1 + \varepsilon_{eng}), \quad (1)$$

$$\varepsilon_{true} = ln(1 + \varepsilon_{eng}), \quad (2)$$

where σ_{eng} is the measured stress; σ_{true} is the true stress; ε_{eng} is the engineering strain; and ε_{true} is the true strain (Zhang et al., 1999). Based on the true stress-strain relationship, a set of plastic strains was calculated by subtracting the elastic strains from the total strains. The plastic strain and stress relationship was used to define the multilinear strain hardening to simulate material nonlinearity. The structural analysis of the pole-mounted structures was limited to the peak stress state of the material. A displacement-controlled method was used in the FEA to a final displacement of 300 mm. The material properties of used materials are included in Table 2.

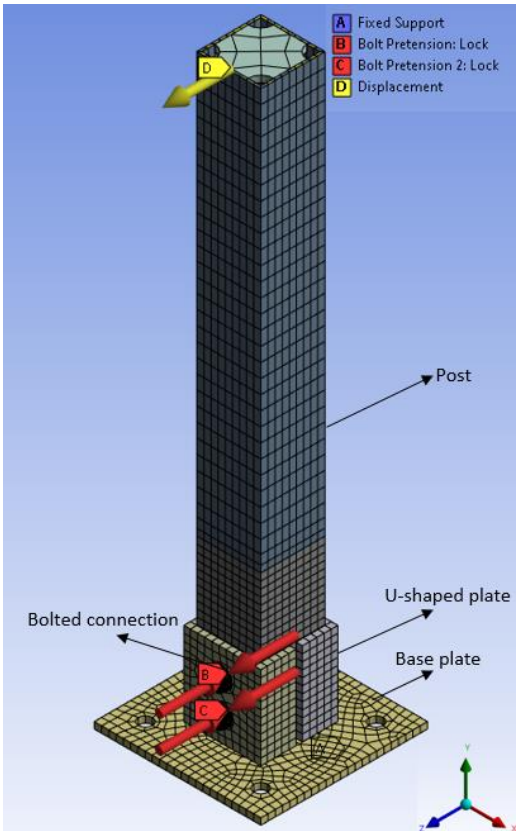

Fig. 3. Mesh generation and boundary conditions of the UC specimen

Table 3. Material properties of the specimens

Components	Yield Strength (MPa)	Ultimate Tensile Strength (MPa)	Elastic modulus (GPa)	Poisson's ratio
Post	384	465	205.5	0.3
Base Plate	293	365	191	0.3
Supporting Plates and Ribs				
Bolts and Nuts	215	505	193	0.3

4. RESULTS

Fig. 4 depicts the load–displacement curves for the plinths with base plate and supporting plate unit. Regarding the welded plinths with base plates, for the WRR specimen, the load initially increased gradually until reaching a peak load of 24.78 kN at 306.7 mm. In contrast, the SWP specimen showed the most brittle behavior among the plinths with base plate, failing at a deflection of 185.19 mm and exhibiting a maximum load of 23.78 kN. The UC specimen exhibited a steady increase in the load until reaching a peak load of 21.76 kN at 255.02 mm. The SC specimen exhibited the most ductile behavior, with a maximum force of 23.69 kN and failure at a displacement of 354.7 mm.

In terms of non-welded plinths with supporting plate units, the URC specimen resisted the highest load of 28.07 kN of all specimens. The TCR specimen bore a maximum load of 27.65 kN with a maximum displacement of 226.59 mm. The BSP specimen exhibited the lowest load-bearing capacity of 17.99 kN, even though the behavior of its load–displacement curve was ductile, with a maximum displacement of 328.06 mm. The TUC and LC specimens showed the best results in terms of ductility, with peak loads of 27.05 kN and 26.29 kN and maximum displacements of 333.23 mm and 353.32 mm.

Two simulations were carried out for the specimens in two loading directions considering the strong and weak axes. Figs. 5 and 6 show a comparison of the simulated and experimental results for the load–displacement relationships of the plinths with base plate and plinths with supporting plate unit, respectively.

As shown in Fig. 5(a), the stiffness of the simulated and experimental results for the WRR specimen is the same at the early stage of loading until a load of 10 kN, after which the stiffness and load of the simulation are greater than those obtained experimentally. This can be attributed to the asymmetrical load applied to the specimens

in the experiments. However, the FEA results for the SWP specimen demonstrated a close correlation with the experimental results, as shown in Fig. 5(b). For the specimens UC and SC, the simulated load–displacement curves were higher than the experimental curves, as shown in Fig. 5(c) and (d). This could be attributed to the perfect bond contact assigned in the FE model to the welded connections, even though the welded parts of the specimens fractured, leading to premature failure.

As shown in Fig. 6(a), the overall load–displacement behavior of the FEA for the URC specimen was also higher than the experimental results. It is supposed that the asymmetrical behavior of the two connected assemblies was the reason for this discrepancy. The simulated load–displacement curve of the TC specimen matched well with the experimental data until the maximum load was reached, after which the analysis was terminated owing to a convergence issue when the bolt holes of the post on the upper backside fractured with large deformation. The initial stiffnesses of the TCR and TUC specimens in the FEA were higher than those of the specimens in the experiments, as shown in Fig. 6(c) and (d). Asymmetrical loading may be the cause of this discrepancy, as in other cases. The simulated results for the BSP and LC specimens, which are shown in Fig. 6(e) and (f), respectively, could effectively capture the load–displacement curves of the specimens with a reasonable correlation.

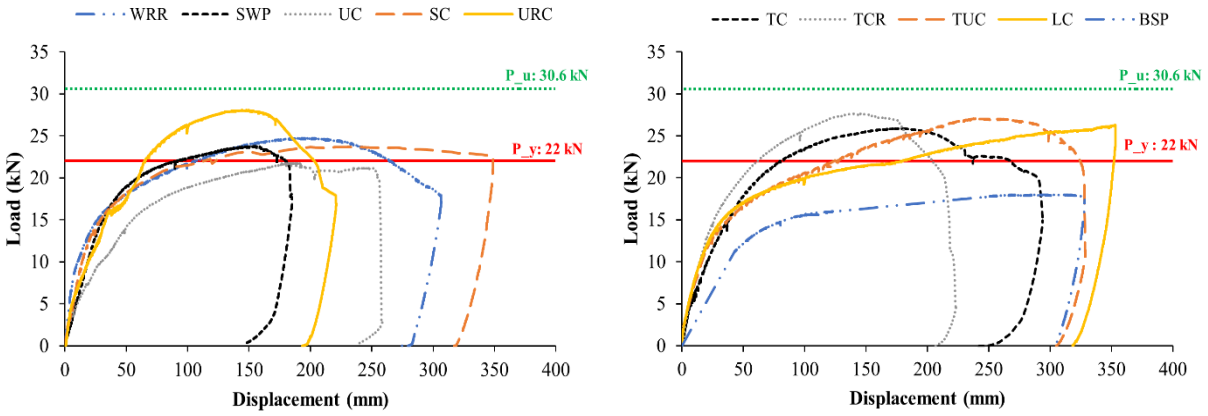

Fig 4. Vertical load vs displacement relationship of plinths (a) with base plate and (b) with supporting plate unit specimens

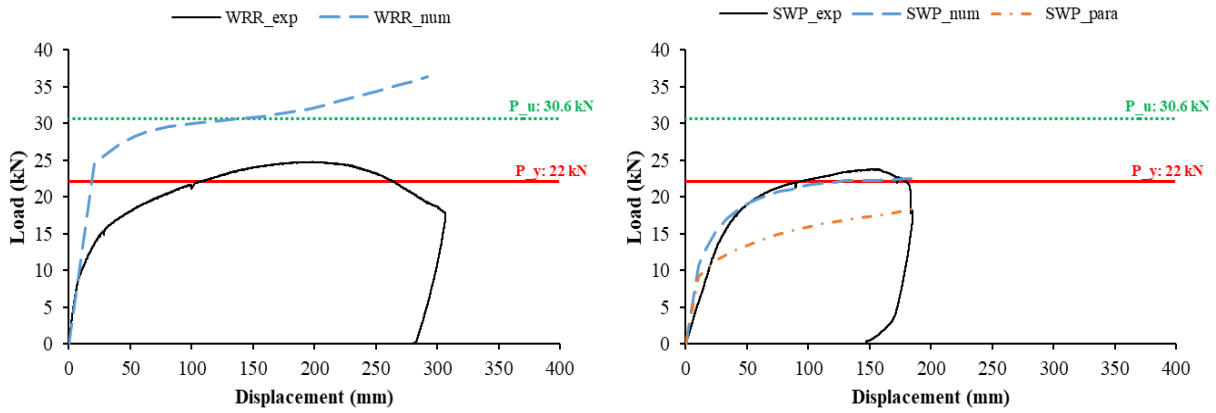

(a) WRR

(b) SWP

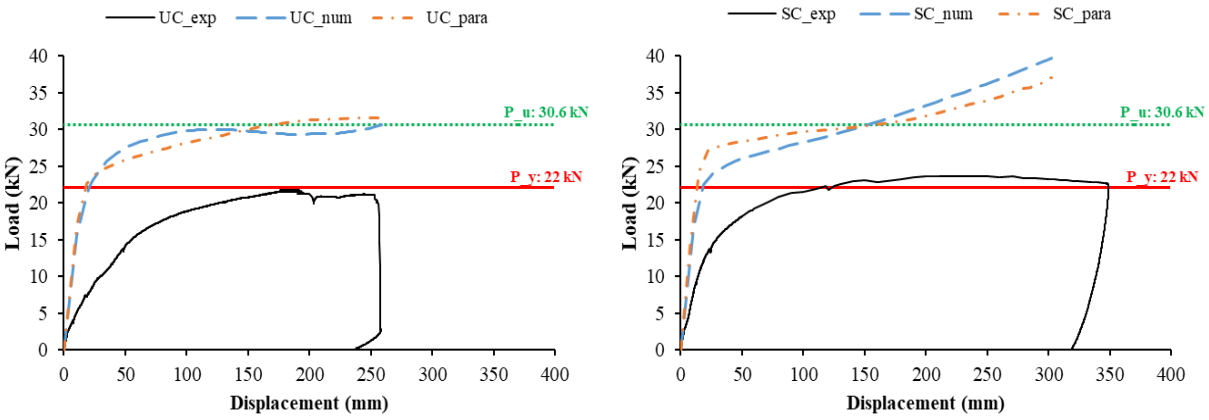

(c) UC

(d) SC

Fig. 5. Vertical load vs displacement relationship comparison between numerical and experimental results of plinths with base plate

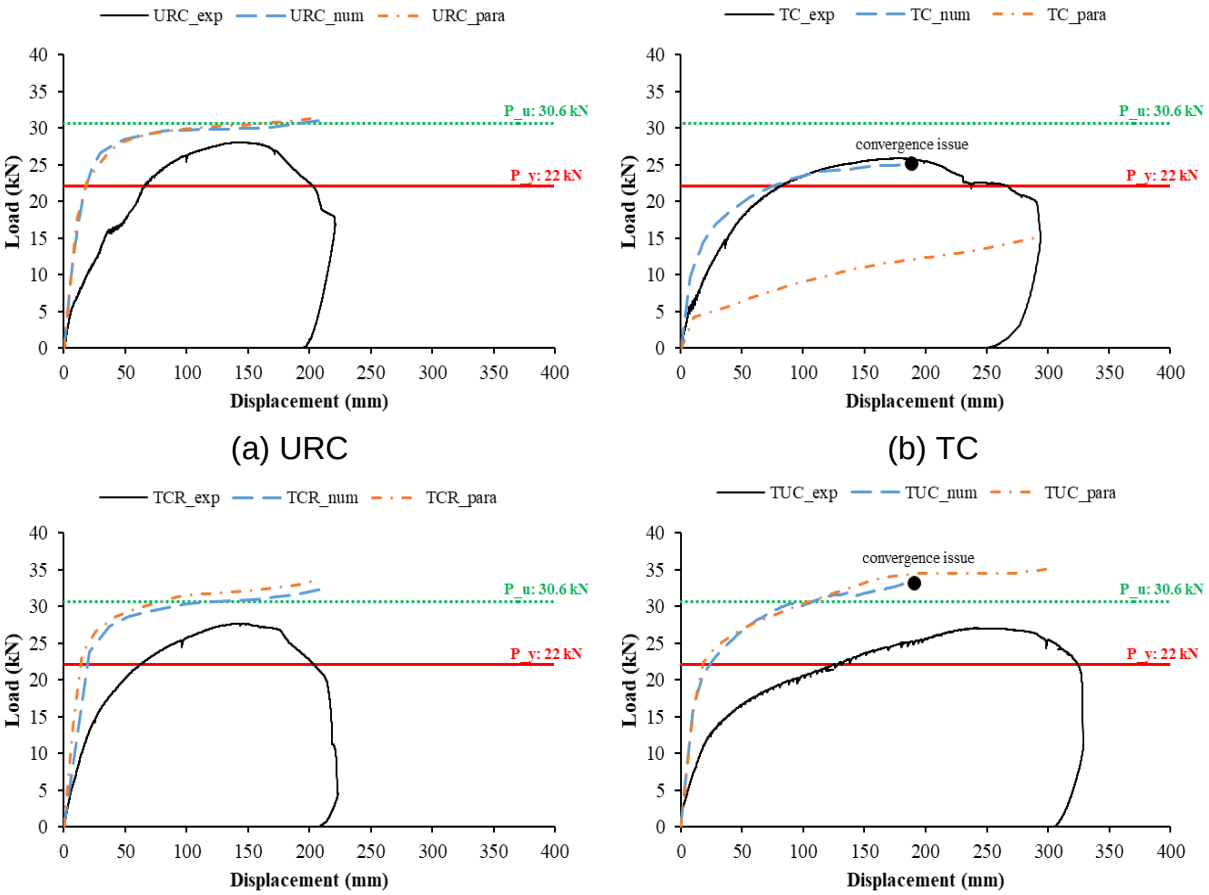

(a) URC

(b) TC

(c) TCR

(d) TUC

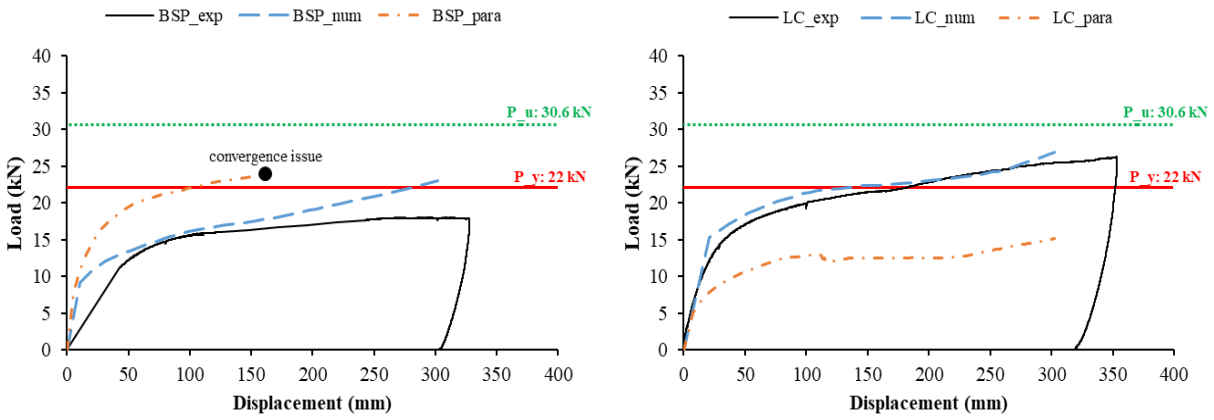

(e) BSP (f) LC

Fig. 6. Vertical load vs displacement relationship comparison between numerical and experimental results of plinths with supporting plate unit

5. DISCUSSION & CONCLUSIONS

Most of the specimens exhibited a higher load-bearing capacity than the calculated yielding force. The failure modes observed in the experimental study included cracking in the welded region, local buckling of the column, and bolt tear-out. Overall, the plinths with supporting plate units were generally more effective in resisting progressively large collapses than the non-welded plinths with base plates; thus, they can be applied to the column–base connections of solar panel structures.

The numerical analysis revealed that the use of rib plates in welded plinth structures caused stress concentration on the column face during buckling. Moreover, the use of bolts in a single column enabled the smooth engagement of the load transfer, whereas the two-column bolted connections caused excessive stress in the web area between the two columns of bolts.

ACKNOWLEDGMENTS

This work was supported by the National Research Foundation of Korea (NRF) grant funded by the Korean government (MSIT) (No. 2021R1C1C2093437).

REFERENCES

Kim, J. M., Kim, T., Son, K., Yum, S. G., Ahn S. (2019). “Measuring Vulnerability of Typhoon in Residential Facilities: Focusing on Typhoon Maemi in South Korea.” Sustainability, 11(10), 2768.

Sohn, I. R., Kim, T. C., Kim, M. S., Kim, J. S., Ju, G. I. (2021). “Anti-Corrosion Performance and Applications of PosMAC® Steel”, Corros Sci, 20(1), 7-14.

Zhang, Z.L., Hauge, M., Ødegård, J., Thaulow, C. (1999). “Determining material true stress–strain curve from tensile specimens with rectangular cross-section.” Int. J. Solids. Struct., 36(23), 3497-3516.